

Intrinsically chiral exciton polaritons in an atomically-thin semiconductor

M. J. Wurdack,^{1,2,3,4,5,*} † I. Iorsh,^{6,†} T. Bucher,^{1,3,4} S. Vavreckova,^{2,3,4}
E. Estrecho,² S. Klimmer,¹ Z. Fedorova,^{1,3,4} H. Deng,⁷ Q. Song,⁷ G. Soavi,^{1,8}
F. Eilenberger,^{3,4,9} T. Pertsch,^{3,4} I. Staude,^{1,3,4} Y. Kivshar,^{10,‡} and E. A. Ostrovskaya^{2,§}

¹*Institute of Solid State Physics, Friedrich Schiller University Jena, 07743 Jena, Germany.*

²*Department of Quantum Science and Technology, Research School of Physics,
The Australian National University, Canberra, ACT 2601, Australia.*

³*Institute of Applied Physics, Friedrich Schiller University Jena, 07745 Jena, Germany.*

⁴*Abbe Center of Photonics, Friedrich Schiller University Jena, 07745 Jena, Germany.*

⁵*Department of Chemical Engineering, Stanford University, Stanford, CA 94305, USA.*

⁶*Department of Physics, Engineering Physics and Astronomy,
Queen's University, Kingston, Ontario, K7L 3N6, Canada.*

⁷*Harbin Institute of Technology, Shenzhen 518055, China.*

⁸*Abbe Center of Photonics, Friedrich Schiller University Jena, 07743 Jena, Germany.*

⁹*Applied Optics and Precision Engineering IOF, Albert-Einstein-Str. 7, 07745 Jena, Germany.*

¹⁰*Nonlinear Physics Center, Research School of Physics,
Australian National University, Canberra ACT 2601, Australia.*

Photonic bound states in the continuum (BICs) have emerged as a versatile tool for enhancing light-matter interactions by strongly confining light fields. Chiral BICs are photonic resonances with a high degree of circular polarisation, which hold great promise for spin-selective applications in quantum optics and nanophotonics. Here, we demonstrate a novel application of a chiral BIC for inducing strong coupling between the circularly polarised photons and spin-polarised (valley) excitons (bound electron-hole pairs) in atomically-thin transition metal dichalcogenide crystals (TMDCs). By placing monolayer WS₂ onto the BIC-hosting metasurface, we observe the formation of intrinsically chiral, valley-selective exciton polaritons, evidenced by circularly polarised photoluminescence (PL) at two distinct energy levels. The PL intensity and degree of circular polarisation of polaritons exceed those of uncoupled excitons in our structure by an order of magnitude. Our microscopic model shows that this enhancement is due to folding of the Brillouin zone creating a direct emission path for high-momenta polaritonic states far outside the light cone, thereby providing a shortcut to thermalisation (energy relaxation) and suppressing depolarisation. Moreover, while the polarisation of the upper polariton is determined by the valley excitons, the lower polariton behaves like an intrinsic chiral emitter with its polarisation fixed by the BIC. Therefore, the spin alignment of the upper and lower polaritons ($\uparrow\downarrow$ and $\uparrow\uparrow$) can be controlled

by σ^+ and σ^- polarised optical excitation, respectively. Our work introduces a new type of chiral light-matter quasi-particles in atomically-thin semiconductors and provides an insight into their energy relaxation dynamics.

Chiral photonic and electronic states are the building blocks for spin-based applications, which include quantum computing and communication, spintronics, and spin-selective sensing. Time-reversal symmetry breaking, parity-time-symmetry breaking or band-gap inversion can induce such chiral states [1–7]. Breaking the symmetry of a metasurface hosting photonic bound states in the continuum (BICs) [8–10] can generate chiral BICs that interact with either σ^+ or σ^- polarised light, i.e., by separating their σ^+ and σ^- polarisation bases in parameter space [1, 5, 11]. Similarly, in semiconducting atomically thin (monolayer) transition-metal dichalcogenide crystals (TMDCs), broken inversion symmetry combined with strong spin-orbit coupling leads to energetically degenerate band edges of the Brillouin zone with alternating spins, where spin-polarised bound electron-hole pairs (excitons) form in the K and K' valleys (see Fig. 1a) [3, 12, 13]. Thus, σ^+ and σ^- polarised light can selectively probe K and K' valley excitons, respectively, which is facilitated by their high oscillator strength and strong photoluminescence (PL) [13–17]. However, experimentally measured degrees of circular polarisation and valley coherence in TMDCs are often much lower than 1 [13, 15, 18–20], mostly due to inelastic scattering events, e.g., with phonons and disorder [17], which strongly limits their potential applications. Scattering can be suppressed by forming exciton polaritons (polaritons herein) in the strong light-matter coupling regime [21], i.e., by placing a TMDC monolayer in a strongly confined light field of a microcavity or a photonic crystal [22]. While polaritons in monolayer TMDCs are well studied [22, 23], these studies are limited to achiral photonic structures, where spin-selective behavior is mainly inherited by the valley-degenerate excitons [24–26].

* mwurdack@stanford.edu

† These authors contributed equally.

‡ yuri.kivshar@anu.edu.au

§ elena.ostrovskaya@anu.edu.au

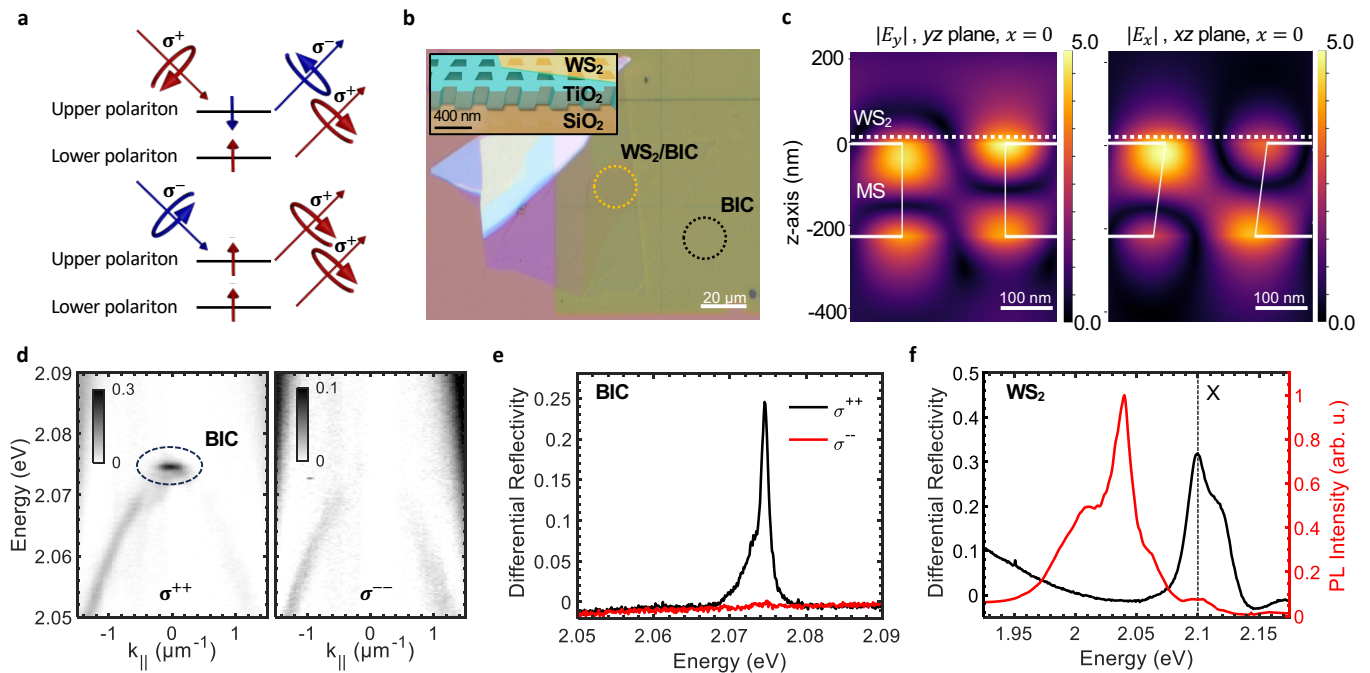


FIG. 1. **Optical properties of the WS_2 /BIC heterostructure.** **a** Schematics of the spin configuration and emission properties of upper and lower polaritons under (top) σ^+ and (bottom) σ^- polarised optical excitation. **b** Microscope image and (inset) schematic illustration of the heterostructure consisting of the metasurface governed by chiral BICs [1] and the monolayer WS_2 . The measured areas are marked with yellow and black circles. **c** Electric field distribution of the metasurface at the BIC resonance wavelength $\lambda = 597$ nm in its linear polarisation bases (left) $|E_y|$ and (right) $|E_x|$ in the yz - and xz -plane, respectively. **d** Angle-resolved differential reflectivity spectra of the metasurface next to the position of the monolayer (black circle in **b**) of (left) σ^+ and (right) σ^- polarised white light, where the reflected light is filtered in its σ^+ and σ^- polarisation bases, respectively. The response of the chiral BIC is marked with a black dashed circle. **e** Polarisation resolved reflectivity spectra of panel **d** plotted along $k = 0$. **f** Reflectivity and photoluminescence spectrum at the position of the monolayer WS_2 (yellow circle in **b**) at $T \approx 4$ K, measured at large momenta ($k_{\parallel} \approx 4.5 \mu\text{m}^{-1}$, see Methods) to avoid the influence of the BIC.

Here, we demonstrate the formation of intrinsically chiral, valley-selective polaritons in a monolayer WS_2 placed on a metasurface governed by chiral BICs [1]. BICs, which are photonic resonances with high Q-factors [8, 9], were recently introduced for achieving polariton formation in a range of materials [27–29]. The choice of material in this work, monolayer WS_2 , is motivated by its spin-valley physics [30] and the ability to reach strong light-matter coupling with the excitons in a wide temperature range, including room temperature [21, 28, 31–33]. We perform experimental and theoretical reflectivity and PL studies showing that, in the strong light-matter coupling regime, diffraction overcomes thermalisation-induced losses and depolarisation, which leads to massively enhanced circularly polarised PL of both the upper and lower polariton branches. Remarkably, lower and upper polaritons can have parallel ($\uparrow\uparrow$) or anti-parallel ($\uparrow\downarrow$) spin-configurations, which can be switched with σ^- or σ^+ polarised excitation, respectively, leading to co- or anti-polarised PL from the two energy levels (see Fig. 1a). This is because both photonic and excitonic constituents of the polaritons contribute to the spin-configurations, with the photonic(excitonic) contribution being stronger

for the lower(upper) polariton. Thus, the lower polariton inherits most of its properties from the chiral BIC, and only interacts with and emits σ^+ polarised light [1]. In contrast, the upper polariton shows rotating dipole behavior as inherited from the exciton, reversing the polarisation of the exciting light [34]. Additionally, the spin degree of freedom of valley excitons also manifests itself in the lower polariton, where the PL is the strongest when the exciton spin is aligned with that of the BIC. As such, combining the spin-selective light and matter states in a hybrid polaritonic state leads to the formation of a new type of chiral bosonic quasiparticle, and offers a novel pathway for the control and manipulation of chiral light emission.

RESULTS

The structure investigated in this work consists of an exfoliated monolayer WS_2 placed on a slant-perturbed metasurface, i.e., a TiO_2 layer deposited on SiO_2 and patterned with a square array of trapezoid nanoholes (see Fig. 1b and Methods) [1]. Good spatial overlap

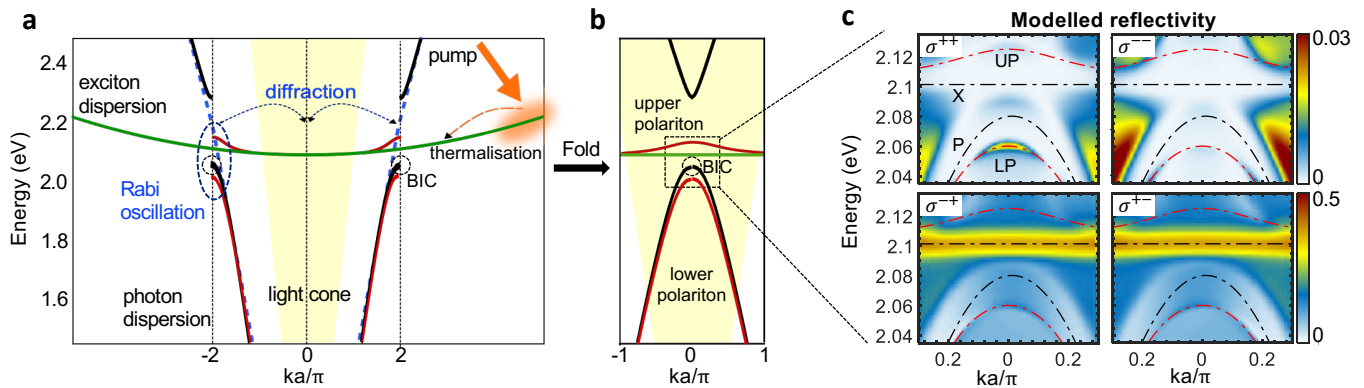


FIG. 2. **Model of exciton-photon coupling.** **a** Dispersion curves of the (black) relevant photonic, (green) excitonic and (red) polaritonic modes of the sample in the strong exciton-photon coupling regime [35], and schematic illustration of relaxation and diffraction processes that lead to photoluminescence. To visualise the parabolic dispersion of the WS₂ exciton ($E_0 \approx 2.1$ eV [16]), the effective mass ($\mu_{eff} \approx 0.2 \cdot m_0$ [36, 37]) is reduced by the factor 20. **b** Folded Brillouin zone of the photonic components, showing that both (green) excitons and (red) polaritons coexist within the light cone. The light cone of our experimental setup (see Methods) is shaded in yellow and the location of the relevant chiral BIC (σ^+) on the photonic dispersion is marked with black dashed circles in panels a,b. **c** Modelled white light reflectivity in the far field, which is dominated by the polariton response (red dashed line) at the native polarisation of the chiral BIC (σ^+), and by the exciton response (X) when the polarisation of the reflected light is opposite to the polarisation of the incoming light (i.e., $\sigma^{+/-+}$). The polariton (UP/LP) and uncoupled exciton/photon (X/P) dispersions are marked as red and black dashed lines, respectively.

between the photonic near-field mode of the metasurface and the monolayer, confirmed by the calculation of the electric field distribution (see Fig. 1c and SI), enables the coupling between the photonic mode and the exciton in the monolayer. The sample is illuminated by either a polarised tungsten-halogen white light source or a continuous-wave (CW) laser tuned to the WS₂ bandgap, and its reflectivity and PL properties are studied in the reflection geometry at cryogenic temperatures ($T \approx 4$ K) (see Methods).

The measured angle-resolved reflectivity spectrum next to the position of the monolayer (see Fig. 1b) shows a discrete mode, which interacts with σ^+ polarised white light at $k_{||} = 0$ and $E \approx 2.075$ eV (see Fig. 1d,e). In particular, this mode (appears)disappears when the sample is illuminated by $(\sigma^+)\sigma^-$ polarised light and the reflected light detected in its $(\sigma^+)\sigma^-$ polarisation basis. This feature marks the optical response of the chiral BIC in our metasurface selective to σ^+ polarised light [1] with a Q-factor of ~ 1500 . Henceforth, σ^{ir} convention indicates polarisations of the incoming (*i*) and reflected (*r*) light. The optical response of the monolayer was characterised via white light reflectivity and PL spectroscopy at large momenta ($k_{||} \approx 4.5 \mu\text{m}^{-1}$) to avoid the influence of the BIC signal prevalent at $k_{||} = 0$ (see Methods). The reflectivity and PL spectra in Fig. 1f show strong excitonic (X) absorption and weak PL emission at $E \approx 2.1$ eV [16], respectively. At 4 K, the PL of dark-type monolayer WS₂ mostly stems from charged and multi-body complexes, e.g., trions, biexcitons and charged biexcitons, which dominate the PL spectrum at lower energies between ~ 1.95 eV and 2.08 eV [30, 38–44]. However, the

prominent exciton resonance in the reflectivity spectrum at ~ 2.1 eV [16], which coincides with the weak exciton PL peak at the same energy, enables strong light-matter interactions and formation of exciton polaritons in this material [33].

To describe the salient features of the optical response in the strong light-matter coupling regime, we plot the dispersion curves of the relevant photonic, excitonic and polaritonic modes in Fig. 2a,b, where the photon and polariton dispersions were calculated with the guided mode expansion method [45] using the exciton parameters derived in Ref. [3]. The periodic structure of the metasurface creates a photonic band gap at $ka/\pi = \pm 2$ (here $k_{||} \approx \pm 18.2 \mu\text{m}^{-1}$ with $a = 340$ nm, see Methods). The BIC is located at the energy maximum of the lower band, which is close to the exciton energy in monolayer WS₂. With sufficiently large energy-exchange interactions, i.e., Rabi oscillation frequencies, level repulsion occurs leading to formation of the upper and the lower polariton branches (see red lines in Fig. 2a). Folding of the Brillouin zone of the metasurface projects the dispersive branches from high-momentum states far outside the light cone of our experimental setup to low-momentum states, e.g., $ka/\pi = \pm 2$ to $ka/\pi = 0$, making the polariton branches visible within the light cone (see Fig. 2b). As such, both excitons (unfolded) and polariton branches (folded) coexist within the light cone. This is in contrast to polaritons in optical microcavities, where in the strong exciton-photon coupling regime the uncoupled excitons are only present far outside of the light cone [35, 46].

When calculating the optical response (reflectivity) of the sample illuminated by circularly polarised white light

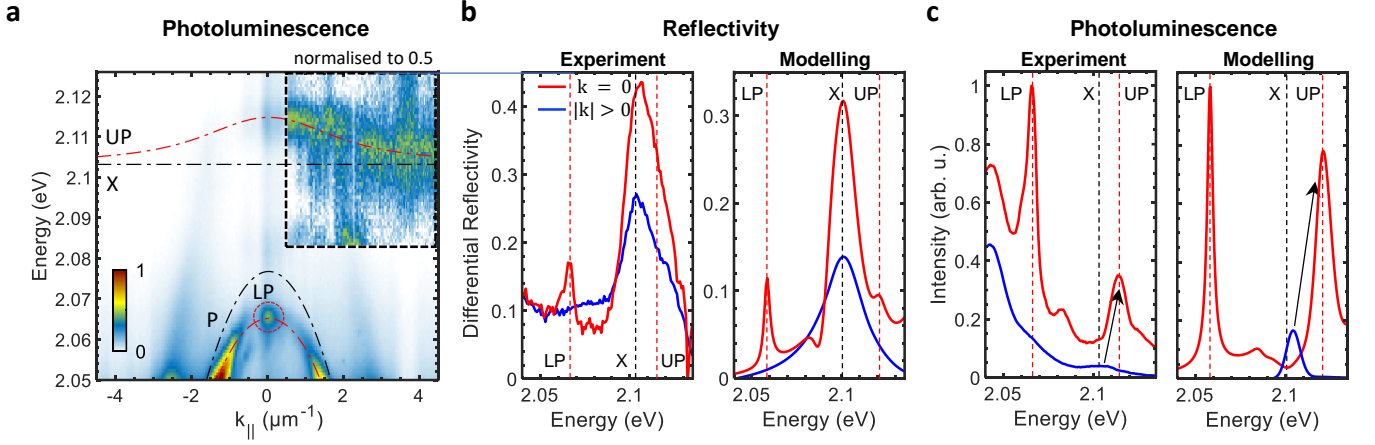


FIG. 3. Reflectivity and photoluminescence spectra. **a** Experimental angle-resolved photoluminescence spectrum, with the fitted (LP) lower and (UP) upper polariton branches (red dashed lines), and the uncoupled (X) exciton and (P) photon dispersions (black dashed lines). The part of the upper polariton dispersion inheriting the chiral BIC properties is marked with a red dashed circle. The data in the inset are normalised to 0.5 for each k_{\parallel} value to visualise the peak positions of the low-intensity upper polariton emission. **b, c** Experimental and theoretical reflectivity and photoluminescence spectra at (red) $k_{\parallel} = 0$ and (blue) $k_{\parallel} \approx 4.5 \mu\text{m}^{-1}$, respectively. The arrows in panel (c) illustrate the order of magnitude enhancement of the PL intensities of the upper polariton between the lower energy state at $k_{\parallel} \approx 4.5 \mu\text{m}^{-1}$ and the higher energy state at $k_{\parallel} = 0$.

(see Methods and Fig. 2c), we find that the lower polariton behaves similarly to the chiral BIC mode, with the reflectivity signal present at σ^{++} and vanishing at σ^{--} (cf. Figs. 1d and 2c, top panels). In contrast, the excitons, which are modeled as rotating dipoles [34], are responsible for the strong reflected signal with the polarisation opposite to that of the illumination $\sigma^{+/-/+}$, which is similar to light reflection at a metallic surface [47]. This can be explained with our band structure (see Fig. 2a), which shows coexistence of excitons and polaritons within the light cone.

To verify our model experimentally, we performed angle-resolved white light reflectivity and PL spectroscopy at the position of the monolayer on the sample (see Fig. 1b). This was done by illuminating the sample with either a white light source or with a 561 nm (2.21 eV) cw-laser, which lies within the band gap of WS_2 ($E_g \approx 2.4$ eV) and quasi-resonantly excites excitons at large momenta. Figure 3a shows the angle-resolved PL intensity of the structure with the peak energies well reproduced by the two coupled oscillator model describing the lower/upper polariton eigenvalues (LP/UP) emerging in the system of a photon (P) strongly coupled to an exciton (X): $E_{\text{LP/UP}} = \frac{1}{2}[E_X + E_P \pm \sqrt{(2\hbar\Omega)^2 + \delta^2}]$ [35], with the exciton-photon energy detuning $\delta = E_X - E_P = 26.4$ meV, and the Rabi splitting $2\hbar\Omega = 42.0$ meV. The excitonic ($|X|^2$) and photonic fractions ($|C|^2$) of polaritons can be described with the corresponding Hopfield coefficients: $|X_{\text{UP/LP}}|^2 = \frac{1}{2}[1 \pm \delta/\sqrt{\delta^2 + 4\hbar^2\Omega^2}]$, $|C_{\text{UP/LP}}|^2 = 1 - |X_{\text{UP/LP}}|^2$ [35], which in our system amount to $|X_{\text{UP/LP}}|^2 \approx 0.76/0.24$ at $k_{\parallel} = 0$. The localised emission peak at $k_{\parallel} = 0$ and $E \approx 2.066$ eV, reminiscent of the chiral BIC response at $E \approx 2.077$ eV (see Fig. 1d), originates from the more photonic LP. The

emission above 2.1 eV corresponds to the more excitonic UP. The UP dispersion near $k_{\parallel} = 0$, when folded as shown in Fig. 2a,b, is strongly modified by level repulsion in proximity to the BIC state causing anti-crossing with the exciton level (X). This confirms the strong coupling regime between the WS_2 excitons and the chiral photonic BIC.

The PL signal, which is dominated by polaritonic states, is in stark contrast to the reflectivity spectrum (see Fig. 3b), which, as predicted by our model (see Fig. 2c), is strongly dominated by the exciton mode. Both high- and low-momenta spectra are well reproduced by our model (see polarisation-resolved spectra in the SI), with the sharp LP peak only present at low momenta (around $k = 0$). This agreement confirms the accuracy of our model, and that both excitons and polaritons coexist within the light cone.

Remarkably, the exciton peak in the PL is strongly suppressed (see Fig. 3a,c). Furthermore, the UP peak is an order of magnitude larger than that of the energetically lower excitonic emission at $k_{\parallel} \approx 4.5 \mu\text{m}^{-1}$ (see Fig. 3c). As thermalisation favors low energy states, the massively enhanced high energy emission contradicts thermalisation as main source of emission at $k_{\parallel} = 0$. To model this behavior, we further leveraged the Green's function approach (see Methods) for calculating the PL emission spectra using the random source approximation [48] (see SI). In the calculation, we used the momentum distribution of the excitonic PL as a fitting parameter to fit the experimentally measured PL spectra. Our model, which shows good agreement with our experimentally obtained data (see Fig. 3b,c) strongly suggests that diffraction is the main source of the polariton PL at $k = 0$, as schematically shown in Fig. 2a. In particular, polari-

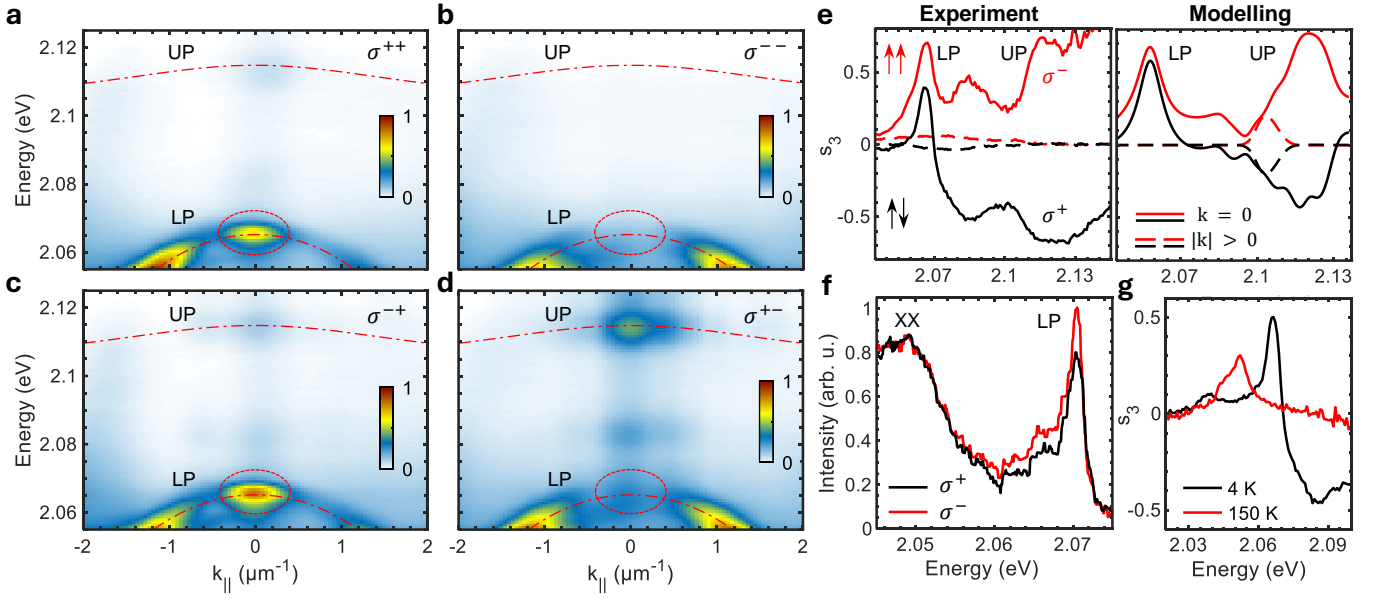


FIG. 4. **Angle- and polarisation-resolved PL spectra.** **a-d** Circularly polarised components of the angle-resolved PL spectra of the sample excited with a circularly polarised laser pump. The σ^{pe} convention reflects the sign of the circular polarisation of the pump (p) and the PL emission (e). **e** Measured and modeled s_3 spectra with (black) σ^- and (red) σ^+ polarised pump. The arrows (\uparrow, \downarrow) mark the spin configurations of the lower and upper polaritons, respectively, under (red) σ^- and (black) σ^+ polarised excitation. **f** PL spectrum of the LP with (black) σ^+ and (red) σ^- polarised pump, with the PL spectra of the biexciton (XX) plotted as reference. **g** s_3 spectra of the LP at (black) $T = 4$ K and (red) $T = 150$ K, respectively.

tons contribute to PL emission within the light cone due to the folding of the Brillouine zone of the metasurface, instead of thermalisation, leading to the observed PL enhancement. The excitons, however, can only relax into the light cone via thermalisation, i.e., inelastic scattering with phonons, which is less efficient. Our findings indicate that this PL mechanism is applicable to polaritons in periodic photonic structures, in general, where diffraction into the light cone can outpace energy relaxation to low momenta states, boosting their quantum yield.

Finally, we investigate the polarisation properties of the polaritons by performing polarisation-resolved PL measurements. Fig. 4a-d shows the circularly polarised components of the momentum-resolved PL spectra (σ^{i+} in Fig. 4a,c and σ^{i-} in Fig. 4b,d) upon excitation with σ^+ (Fig. 4a,d) or σ^- (Fig. 4b,c) polarised light. Remarkably, at $k = 0$, the LP emission is for both circular polarisations of the pump σ^+ polarised (Fig. 4a,c), as defined by the polarisation of the chiral BIC as seen in Fig. 1d. The polarisation of the UP, however, is opposite to that of the pump, both in σ^{+-} and σ^{-+} configurations, which is reminiscent of the rotating dipole behavior of the exciton. This is because the LP ($|C|^2 = 0.76$ at $k_{||} = 0$) mostly inherits the properties of the chiral photonic BIC state, while the UP ($|X|^2 = 0.76$ at $k_{||} = 0$) behaves more like a valley exciton. Consequently, the emitted light of the UP and LP have opposite(same) signs of circular polarisations at $k = 0$ under $\sigma^+(\sigma^-)$ polarised excitation.

We further analyse the antisymmetric polarisation behavior by calculating the $s_3 = (I^+ - I^-)/(I^+ + I^-)$ spec-

tra for both circular polarisations (σ^+ and σ^-) of the pump (see Fig. 4e). Here, UP and LP reach values of $s_3 > +0.7$ with σ^- polarised excitation, and $s_3 \approx -0.7$ for the UP and $s_3 \approx +0.4$ for the LP with σ^+ polarised excitation. Interestingly, s_3 completely vanishes at large momenta, where the emitting states are mostly excitonic. This strong suppression of s_3 is likely a result of inelastic scattering processes required for relaxation (thermalisation) of excitons into the light cone. At $k = 0$, the strong enhancement of circular polarisation is well reproduced by our model, indicating that, in addition to boosting PL intensity, diffraction also strongly enhances polarisation of the polaritons by bypassing the inelastic scattering processes. In combination with the contribution from the intrinsically chiral BIC, it leads to the strong antisymmetric polarisation of the UP and LP, where changing the polarisation of the pump laser triggers switching between parallel ($\uparrow\uparrow$) and anti-parallel ($\uparrow\downarrow$) spin configurations of the two polariton states (see Fig. 1a).

The role of the matter component (the valley exciton) in the chiral BIC-like lower polariton becomes evident when measuring the absolute intensity of its PL under circularly polarised excitation. We find that the quantum yield is the strongest when the spin of the valley exciton is aligned with the polarisation of the chiral BIC (see Fig. 4f). The reference spectrum produced by the uncoupled biexciton (XX) [41], on the other hand, shows no enhancement. Further, the matter-component of the LP enables effective interaction with phonons, as shown in the temperature-dependent measurements (see

Fig. 4g), where both the energy and degree of circular polarisation drop with increasing phonon energies. These results demonstrate that by strongly coupling chiral BIC photons with valley excitons, we successfully created an intrinsically chiral hybrid state that possesses valley physics and effectively interacts with the surrounding medium, further distinguishing our findings from previous investigations of weakly coupled excitons [5].

In summary, by strongly coupling valley excitons with chiral photonic BICs, we have created a new type of chiral hybrid quasi-particles, whose two energy eigenstates can possess distinct spin configurations, either parallel ($\uparrow\uparrow$) or anti-parallel ($\uparrow\downarrow$), depending on the circular polarisation of the optical excitation source (see Fig. 1a). By combining the unique physics of a chiral photonic and a spin-valley electronic system, we therefore complemented the portfolio of spin-selective chiral states with a light-matter hybrid particle with optically controllable spin properties. The potential for ultrafast optical switching between $\uparrow\uparrow$ and $\uparrow\downarrow$ spin configurations in response to polarised light can be useful for spintronics, spin-based transistors, and chiral sensors.

Methods: To make the metasurface, we deposited a 220 nm TiO_2 layer on a glass (SiO_2) substrate by electron beam evaporation (0.065 nm/s). The TiO_2 layer was then patterned using electron-beam lithography. This was done by depositing 20 nm of Cr and spin-coating a 80 nm thick film of PMMA. The PMMA was patterned using electron beam lithography, and the pattern then etched into the Cr layer with inductively coupled Cl_2 and O_2 plasma. Further, we etched the TiO_2 layer in a slant-etching system (as developed in [1]) with reactive O_2 , SF_6 , Ar and CHF_3 ions. Finally, the PMMA was removed with Acetone. With this process, we created the slant-perturbed TiO_2 metasurface consisting of a square array of trapezoid nanoholes, with the parameters: unit cell size $a = 340$ nm, width of hole $w = 210$ nm, height of hole $h = 220$ nm, slant angle $\phi = 0.1$ and in-plane deformation angle $\alpha = 0.12$, as presented in [1] and schematically shown in Fig. 1b. The monolayer WS_2 was mechanically exfoliated from a bulk WS_2 crystal (sourced from HQ graphene) onto a gel-film (Gel Pak), and transferred onto the metasurface using the dry transfer technique.

The dispersion of the polaritonic modes was calculated using guided mode expansion method [45], which is particularly useful for calculation of the dispersion of the resonant modes characterized by long radiative lifetimes but can not be used to evaluate the non-resonant reflection from the metasurface.

The reflectivity of the sample was calculated using the rigorous coupled wave analysis (RCWA) [49]. The RCWA method allows us to calculate both the angular and frequency spectra of the polarisation-resolved reflection coefficient and the total scattering matrix $S^{\mathbf{Q}\mathbf{Q}'}$ connecting the multiple diffraction orders of the incoming and outgoing waves $\mathbf{E}^{\mathbf{Q}} = S^{\mathbf{Q}\mathbf{Q}'} \mathbf{E}^{\mathbf{Q}'}$, where \mathbf{Q} index la-

bels different diffraction orders. The scattering matrix is also used to calculate the dyadic Green's function of the metasurface, which we employ for calculating the PL emission spectra of our structure (see SI).

The PL and reflectivity measurements were conducted in a closed-cycle helium cryostat (Montana Instruments s50). For the PL measurements, the sample was excited with a 561 nm wavelength continuous-wave diode-pumped solid-state laser at a power of $30\mu\text{W}$. The source for the reflectivity measurements was a stabilised tungsten-halogen white light source. The laser or white light was focused with a high-NA objective (100x/0.9 NA) onto the sample surface, creating a light spot size of $0.45\mu\text{m}$ in the focus of the objective. The reflected or emitted light from our structure was separated from the incoming light by a non-polarising 30:70 beam splitter cube, and collected with an array of lenses in a 4-f arrangement, where the back focal plane was focused onto the spectrometer slit of an Andor Shamrock i750 spectrograph, equipped with an Andor iXon 897 Ultra EMCCD camera, for imaging the presented momentum-resolved spectra. By employing a spatial filter in the real space image of our 4f-setup, we ensured that only the light stemming from the marked areas in Fig. 1b is collected and analysed. The presented reflectivity data were obtained by differential reflectance spectroscopy $\Delta R/R_{Ref} = (R - R_{Ref})/R_{Ref}$, using the reflectivity spectrum of the TiO_2 coated glass surface next to the metasurface as a reference (Ref). For the polarisation-resolved measurements, we prepared the polarisation of the excitation beam with a linear polariser and quarter-wave phase plate. The polarisation of the detected light was analysed by a combination of superachromatic quarter-wave phase plate and a linear polariser. To increase the signal-to-noise ratio in the presented polarisation-resolved images (4a-d), we performed a moving average calculation in momentum space, effectively applying the average of 9 neighboring pixels along $k_{||}$ to each pixel.

Data availability: The data that support the findings of this study are available from the corresponding authors upon reasonable request.

Acknowledgements: This work was funded by the Australian Research Council (grants CE170100039, DP210101292 and DE220100712), the Deutsche Forschungsgemeinschaft (DFG, German Research Foundation) - CRC/SFB 1375 NOA "Nonlinear Optics down to Atomic scales" (Project number 398816777), the International Research Training Group 2675 "META-Active" (project number 437527638) and the International Technology Center Indo-Pacific (ITC IPAC) via Army Research Office (contract FA520923C0023). M.W. acknowledges support by Schmidt Science Fellows, in partnership with Schmidt Sciences and Rhodes Trust. The authors thank Mikhail Glazov for fruitful discussions.

-
- [1] Y. Chen, H. Deng, X. Sha, W. Chen, R. Wang, Y.-H. Chen, J. C. Dong Wu, Y. S. Kivshar, S. Xiao, and C.-W. Qiu, Observation of intrinsic chiral bound states in the continuum, *Nature* **613**, 474–478 (2023).
- [2] M. König, S. Wiedmann, C. Brune, A. Roth, H. Buhmann, L. W. Molenkamp, X.-L. Qi, and S.-C. Zhang, Quantum spin hall insulator state in hgte quantum wells, *Science* **318**, 766 (2007).
- [3] D. Xiao, G.-B. Liu, X. X. Wanxiang Feng, and W. Yao, Coupled spin and valley physics in monolayers of mos2 and other group-vi dichalcogenides, *Phys. Rev. Lett.* **108**, 196802 (2012).
- [4] M. Mancini, G. Pagano, G. Cappellini, L. Livi, M. Rider, J. Catani, C. Sias, P. Zoller, M. Inguscio, M. Dalmonte, and L. Fallani, Observation of chiral edge states with neutral fermions in synthetic hall ribbons, *Science* **349**, 1510 (2015).
- [5] X. Zhang, Y. Liu, J. Han, Y. Kivshar, and Q. Song, Chiral emission from resonant metasurfaces, *Science* **377**, 1215 (2022).
- [6] T. Gao, G. Li, E. Estrecho, T. Liew, D. Comber-Todd, A. Nalitov, M. Steger, K. West, L. Pfeiffer, D. Snoke, , A. Kavokin, A. Truscott, and E. Ostrovskaya, Chiral modes at exceptional points in exciton-polariton quantum fluids, *Physical review letters* **120**, 065301 (2018).
- [7] R. Su, E. Estrecho, D. Biegańska, Y. Huang, M. Wurdack, M. Pieczarka, A. G. Truscott, T. C. Liew, E. A. Ostrovskaya, and Q. Xiong, Direct measurement of a non-hermitian topological invariant in a hybrid light-matter system, *Science Advances* **7**, eabj8905 (2021).
- [8] D. C. Marinica, A. G. Borisov, and S. V. Shabanov, Bound states in the continuum in photonics, *Phys. Rev. Lett.* **100**, 183902 (2008).
- [9] K. Koshelev, S. Lepeshov, M. Liu, A. Bogdanov, and Y. Kivshar, Asymmetric metasurfaces with high- q resonances governed by bound states in the continuum, *Phys. Rev. Lett.* **121**, 193903 (2018).
- [10] L. Kühner, F. J. Wendisch, A. A. Antonov, J. Bürger, L. Hüttenhofer, L. de S. Menezes, S. A. Maier, M. V. Gorkunov, Y. Kivshar, and A. Tittl, Unlocking the out-of-plane dimension for photonic bound states in the continuum to achieve maximum optical chirality, *Light: Science & Applications* **12**, 250 (2023).
- [11] W. Lv, H. Qin, Z. Su, C. Zhang, J. Huang, Y. Shi, B. Li, P. Genevet, and Q. Song, Robust generation of intrinsic c points with magneto-optical bound states in the continuum, *Science Advances* **10**, eads0157 (2024).
- [12] H. Yu, X. Cui, X. Xu, and W. Yao, Valley excitons in two-dimensional semiconductors, *National Science Review* **2**, 57 (2015).
- [13] G. Wang, A. Chernikov, M. M. Glazov, T. F. Heinz, X. Marie, T. Amand, and B. Urbaszek, Excitons in atomically thin transition metal dichalcogenides, *Rev. Mod. Phys.* **90**, 021001 (2018).
- [14] K. F. Mak, C. Lee, J. Hone, J. Shan, and T. F. Heinz, Atomically thin MoS₂: A new direct-gap semiconductor, *Phys. Rev. Lett.* **105**, 136805 (2010).
- [15] H. Zeng, J. Dai, W. Yao, D. Xiao, and X. Cui, Valley polarization in MoS₂ monolayers by optical pumping, *Nature Nanotechnology* **7**, 490–493 (2012).
- [16] A. Chernikov, T. C. Berkelbach, H. M. Hill, A. Rigosi, Y. Li, B. Aslan, D. R. Reichman, M. S. Hybertsen, and T. F. Heinz, Exciton binding energy and nonhydrogenic rydberg series in monolayer WS₂, *Physical Review Letters* **113**, 076802 (2014).
- [17] G. Gupta, K. Watanabe, T. Taniguchi, and K. Majumdar, Observation of 100% valley-coherent excitons in monolayer MoS₂ through giant enhancement of valley coherence time, *Light: Science & Applications* **12**, 173 (2023).
- [18] K. F. Mak, K. He, J. Shan, and T. F. Heinz, Control of valley polarization in monolayer MoS₂ by optical helicity, *Nature Nanotechnology* **7**, 494 (2012).
- [19] M. M. Glazov, E. L. Ivchenko, G. Wang, T. Amand, X. Marie, B. Urbaszek, and B. L. Liu, Spin and valley dynamics of excitons in transition metal dichalcogenide monolayers, *physica status solidi (b)* **252**, 2349 (2015).
- [20] K. F. Mak and J. Shan, Photonics and optoelectronics of 2D semiconductor transition metal dichalcogenides, *Nature Photonics* **10**, 216 (2016).
- [21] M. Wurdack, E. Estrecho, S. Todd, T. Yun, M. Pieczarka, S. K. Earl, J. A. Davis, C. Schneider, A. G. Truscott, and E. A. Ostrovskaya, Motional narrowing, ballistic transport, and trapping of room-temperature exciton polaritons in an atomically-thin semiconductor, *Nature Communications* **12**, 5366 (2021).
- [22] C. Schneider, M. M. Glazov, T. Korn, S. Höfling, and B. Urbaszek, Two-dimensional semiconductors in the regime of strong light-matter coupling, *Nature Communications* **9**, 2695 (2024).
- [23] Y. Luo, J. Zhao, A. Fieramosca, Q. Guo, H. Kang, X. Liu, T. C. H. Liew, D. Sanvitto, Z. An, S. Ghosh, Z. Wang, H. Xu, and Q. Xiong, Strong light-matter coupling in van der waals materials, *Light: Science and Applications* **13**, 203 (2024).
- [24] Y.-J. Chen, J. D. Cain, T. K. Stanev, V. P. Dravid, and N. P. Stern, Valley-polarized exciton-polaritons in a monolayer semiconductor, *Nature Photonics* **11**, 431–435 (2017).
- [25] S. Dufferwiel, T. P. Lyons, D. D. Solnyshkov, A. A. Trichet, F. Withers, S. Schwarz, G. Malpuech, J. M. Smith, K. S. Novoselov, M. S. Skolnick, D. N. Krizhanovskii, and A. I. Tartakovskii, Valley-addressable polaritons in atomically thin semiconductors, *Nature Photonics* **11**, 497 (2017).
- [26] N. Lundt, Łukasz Dusanowski, E. Sedov, P. Stepanov, M. M. Glazov, S. Klembt, M. Klaas, J. Beierlein, Y. Qin, S. Tongay, M. Richard, A. V. Kavokin, S. Höfling, and C. Schneider, Optical valley Hall effect for highly valley-coherent exciton-polaritons in an atomically thin semiconductor, *Nature Nanotechnology* **14**, 770 (2019).
- [27] V. Ardizzone, F. Riminucci, S. Zanotti, A. Gianfrate, M. Eftymiou-Tsironi, D. G. Suárez-Forero, F. Todisco, M. D. Giorgi, D. Trypogeorgos, G. Gigli, K. Baldwin, L. Pfeiffer, D. Ballarini, H. S. Nguyen, D. Gerace, , and D. Sanvitto, Polariton bose-einstein condensate from a bound state in the continuum, *Nature* **605**, 447–452 (2022).
- [28] E. Maggiolini, L. Polimeno, F. Todisco, A. D. Renzo, B. Han, M. D. Giorgi, R. M. Vincenzo Ardizzone, Christian Schneider, A. Cannavale, M. Pugliese, L. D. Marco, A. Rizzo, V. Maiorano, G. Gigli, D. Gerace, D. Sanvitto,

- and D. Ballarini, Strongly enhanced light–matter coupling of monolayer WS₂ from a bound state in the continuum, *Nature Materials* **22**, 964–969 (2023).
- [29] X. Wu, S. Zhang, J. Song, X. Deng, W. Du, X. Zeng, Y. Zhang, Z. Zhang, Y. Chen, Y. Wang, C. Jiang, Y. Zhong, B. Wu, Z. Zhu, Y. Liang, Q. Zhang, Q. Xiong, and X. Liu, Exciton polariton condensation from bound states in the continuum at room temperature, *Nature Communications* **15**, 3345 (2024).
- [30] G. Plechinger, P. Nagler, A. Arora, R. Schmidt, A. Chernikov, A. G. D. Águila, P. C. Christianen, R. Bratschitsch, C. Schüller, and T. Korn, Trion fine structure and coupled spin-valley dynamics in monolayer tungsten disulfide, *Nature Communications* **7**, 12715 (2016).
- [31] L. C. Flatten, Z. He, D. M. Coles, A. A. Trichet, A. W. Powell, R. A. Taylor, J. H. Warner, and J. M. Smith, Room-temperature exciton-polaritons with two-dimensional WS₂, *Scientific Reports* **6**, 33134 (2016).
- [32] L. Zhang, R. Gogna, W. Burg, E. Tutuc, and H. Deng, Photonic-crystal exciton-polaritons in monolayer semiconductors, *Nature Communications* **9**, 713 (2018).
- [33] J. Zhao, A. Fieramosca, R. Bao, W. Du, K. Dini, R. Su, J. Feng, Y. Luo, D. Sanvitto, T. C. H. Liew, and Q. Xiong, Nonlinear polariton parametric emission in an atomically thin semiconductor based microcavit, *Nature Nanotechnology* **17**, 396 (2022).
- [34] T. Bucher, Z. Fedorova, M. Abasifard, M. J. W. Rajeshkumar Mupparapu, E. Najafidehaghani, Z. Gan, H. Knopf, A. George, F. Eilenberger, T. Pertsch, A. Turchanin, and I. Staude, Influence of resonant plasmonic nanoparticles on optically accessing the valley degree of freedom in 2d semiconductors, *Nature Communications* **15**, 10098 (2024).
- [35] H. Deng, H. Haug, and Y. Yamamoto, Exciton-polariton Bose-Einstein condensation, *Rev. Mod. Phys.* **82**, 1489 (2010).
- [36] A. Ramasubramaniam, Large excitonic effects in monolayers of molybdenum and tungsten dichalcogenides, *Phys. Rev. B* **86**, 115409 (2012).
- [37] M. Goryca, J. Li, A. V. Stier, T. Taniguchi, K. Watanabe, E. Courtade, S. Shree, C. Robert, B. Urbaszek, X. Marie, and S. A. Crooker, Revealing exciton masses and dielectric properties of monolayer semiconductors with high magnetic fields, *Nature Communications* **10**, 4172 (2019).
- [38] T. Mueller and E. Malic, Exciton physics and device application of two-dimensional transition metal dichalcogenide semiconductors, *npj 2D Materials and Applications* **2**, 28 (2018).
- [39] M. A. Conway, J. B. Muir, S. K. Earl, M. Wurdack, R. Mishra, J. O. Tollerud, and J. A. Davis, Direct measurement of biexcitons in monolayer WS₂, *2D Materials* **9**, 021001 (2022).
- [40] S. Y. Chen, T. Goldstein, T. Taniguchi, K. Watanabe, and J. Yan, Coulomb-bound four- and five-particle intervalley states in an atomically-thin semiconductor, *Nature Communications* **9**, 3717 (2018).
- [41] P. Nagler, M. V. Ballottin, A. A. Mitioglu, M. V. Durnev, T. Taniguchi, K. Watanabe, A. Chernikov, C. Schüller, M. M. Glazov, P. C. M. Christianen, and T. Korn, Zeeman splitting and inverted polarization of biexciton emission in monolayer WS₂, *Phys. Rev. Lett.* **121**, 057402 (2018).
- [42] A. Singh, K. Tran, M. Kolarczik, J. Seifert, Y. Wang, K. Hao, D. Pleskot, N. M. Gabor, S. Helmrich, N. Owschimikow, U. Woggon, and X. Li, Long-lived valley polarization of intravalley trions in monolayer WSe₂, *Phys. Rev. Lett.* **117**, 257402 (2016).
- [43] Z. Ye, L. Waldecker, E. Y. Ma, D. Rhodes, A. Antony, B. Kim, X. X. Zhang, M. Deng, Y. Jiang, Z. Lu, D. Smirnov, K. Watanabe, T. Taniguchi, J. Hone, and T. F. Heinz, Efficient generation of neutral and charged biexcitons in encapsulated WSe₂ monolayers, *Nature Communications* **9**, 3718 (2018).
- [44] Y. You, X. X. Zhang, T. C. Berkelbach, M. S. Hybertsen, D. R. Reichman, and T. F. Heinz, Observation of biexcitons in monolayer WSe₂, *Nature Physics* **11**, 477 (2015).
- [45] S. Zanotti, H. S. Nguyen, M. Minkov, L. C. Andreani, and D. Gerace, Theory of photonic crystal polaritons in periodically patterned multilayer waveguides, *Phys. Rev. B* **106**, 115424 (2022).
- [46] T. Byrnes, N. Y. Kim, and Y. Yamamoto, Exciton-polariton condensates, *Nature Physics* **10**, 803 (2014).
- [47] G. Scuri, Y. Zhou, A. A. High, D. S. Wild, C. Shu, K. De Greve, L. A. Jauregui, T. Taniguchi, K. Watanabe, P. Kim, M. D. Lukin, and H. Park, Large excitonic reflectivity of monolayer MoSe₂ encapsulated in hexagonal boron nitride, *Phys. Rev. Lett.* **120**, 037402 (2018).
- [48] L. Deych, M. Erementchouk, A. Lisyansky, E. Ivchenko, and M. Voronov, Exciton luminescence in one-dimensional resonant photonic crystals: A phenomenological approach, *Physical Review B—Condensed Matter and Materials Physics* **76**, 075350 (2007).
- [49] J. Schlipf and I. A. Fischer, Rigorous coupled-wave analysis of a multi-layered plasmonic integrated refractive index sensor, *Optics Express* **29**, 36201 (2021).

Supplementary Information

Intrinsically chiral exciton polaritons in an atomically-thin semiconductor

M. J. Wurdack,^{1,2,3,4,5,*} † I. Iorsh,^{6,†} T. Bucher,^{1,3,4} S. Vavreckova,^{2,3,4}
 E. Estrecho,² S. Klimmer,¹ Z. Fedorova,^{1,3,4} H. Deng,⁷ Q. Song,⁷ G. Soavi,^{1,8}
 F. Eilenberger,^{3,4,9} T. Pertsch,^{3,4} I. Staudé,^{1,3,4} Y. Kivshar,^{10,‡} and E. A. Ostrovskaya^{2,§}

¹*Institute of Solid State Physics, Friedrich Schiller University Jena, 07743 Jena, Germany.*

²*Department of Quantum Science and Technology, Research School of Physics,
The Australian National University, Canberra, ACT 2601, Australia.*

³*Institute of Applied Physics, Friedrich Schiller University Jena, 07745 Jena, Germany.*

⁴*Abbe Center of Photonics, Friedrich Schiller University Jena, 07745 Jena, Germany.*

⁵*Department of Chemical Engineering, Stanford University, Stanford, CA 94305, USA.*

⁶*Department of Physics, Engineering Physics and Astronomy,
Queen's University, Kingston, Ontario, K7L 3N6, Canada.*

⁷*Harbin Institute of Technology, Shenzhen 518055, China.*

⁸*Abbe Center of Photonics, Friedrich Schiller University Jena, 07743 Jena, Germany.*

⁹*Applied Optics and Precision Engineering IOF, Albert-Einstein-Str. 7, 07745 Jena, Germany.*

¹⁰*Nonlinear Physics Center, Research School of Physics,
Australian National University, Canberra ACT 2601, Australia.*

Theory: The metasurface is a structure with discrete translational invariance. The in-plane component of the wavevector is conserved modulo reciprocal lattice vectors \mathbf{Q} . In the systems with continuous translational invariance we could express the electric field vector $\mathbf{E}_{\mathbf{k}}$ as

$$\mathbf{E}_{\mathbf{k}}(z) = \int dz' G_{\mathbf{k}}(z, z') \mathbf{P}_{\mathbf{k}}(z'), \quad (1)$$

where \mathbf{k} is the in-plane wavevector, \mathbf{P} is the polarization at specific wavevector and specific position along the z axis. In the system with discrete translational invariance we instead should write

$$\mathbf{E}_{\mathbf{k}+\mathbf{Q}}(z) = \int dz' G_{\mathbf{k}}^{\mathbf{Q},\mathbf{Q}'}(z, z') \mathbf{P}_{\mathbf{k}+\mathbf{Q}'}(z'), \quad (2)$$

where \mathbf{Q}, \mathbf{Q}' span over all the reciprocal lattice vectors and the summation is taken over the repeating indices \mathbf{Q}' . For each specific values of \mathbf{k}, z, z' , G is the matrix consisting of 3×3 blocks labeled by \mathbf{Q} and \mathbf{Q}' which connect the 3 electric field components with momenta $\mathbf{k} + \mathbf{Q}$ and at position z to the polarization with momenta $\mathbf{k} + \mathbf{Q}'$ at position z' . In our analysis we will only consider in-plane polarization induced by excitons and model in-plane components of the emitted electric field, and therefore we can only consider 2×2 blocks.

We assume that the monolayer is placed at the $z = 0$ plane and that both incident and emitted radiation is in the $z > 0$ half space. For further analysis we will need the Green's functions corresponding to $z = z' = 0$ and to $z \rightarrow \infty, z' = 0$. While the former connects the

polarization at the plane of the monolayer to the electric field at the same plane, the latter connects the monolayer polarization to the far field which is ultimately detected in the experiment.

The Green's function can be expressed via the reflection matrix \hat{r} :

$$G_{\mathbf{k}}^{\mathbf{Q},\mathbf{Q}'}(0, 0) = [\hat{I} + \hat{r}] \cdot [\delta_{\mathbf{Q},\mathbf{Q}'} \otimes G_{0,\mathbf{k}+\mathbf{Q}}], \quad (3)$$

where \hat{I} is the identity matrix, G_0 is the Green's function for the free space:

$$G_{0,\mathbf{k}+\mathbf{Q}} = \frac{i}{2k_0^2 k_z} \begin{pmatrix} k_0^2 - k_x^2 & -k_x k_y \\ -k_x k_y & k_0^2 - k_y^2 \end{pmatrix}, \quad (4)$$

and \hat{r} is the reflection consisting of 2×2 blocks

$$\hat{r}^{\mathbf{Q},\mathbf{Q}'} = \begin{pmatrix} r_{xx}^{\mathbf{Q},\mathbf{Q}'} & r_{xy}^{\mathbf{Q},\mathbf{Q}'} \\ r_{yx}^{\mathbf{Q},\mathbf{Q}'} & r_{yy}^{\mathbf{Q},\mathbf{Q}'} \end{pmatrix} \quad (5)$$

The reflection matrix is computed numerically using the rigorous coupled wave analysis (RCWA) [1]. We note that RCWA allows to calculate the generalized transfer matrices in the whole structure which in turn can be used to restore the local field distributions. The electric field distribution at the wavelength of the chiral BIC $\lambda \approx 597$ nm maps in three orthogonal planes are shown in Fig. 1.

The polarization of excitons $\mathbf{P}_{\mathbf{q}}(z, t) = \mathbf{P}_{\mathbf{q}}(t)\delta(z)$ satisfies the equation:

$$\dot{\mathbf{P}}_{\mathbf{q}}(t) = (-i\omega_X(\mathbf{q}) - \Gamma - i\frac{1}{2}\Omega_{\mathbf{q}}\sigma)\mathbf{P}_{\mathbf{q}} - \quad (6)$$

$$\gamma\mathbf{E}_{\mathbf{q}}(z = 0, t) + \chi_{\mathbf{q}}(t), \quad (7)$$

where ω_X, Γ are the frequency and non-radiative rates of excitons, $\Omega_{\mathbf{q}}$ is the effective exciton magnetic field due to the TE-TM exciton splitting, γ is the excitonic radiative decay rate, and χ is the exciton pumping rate from

* mwurdack@stanford.edu

† These authors contributed equally.

‡ yuri.kivshar@anu.edu.au

§ elena.ostrovskaya@anu.edu.au

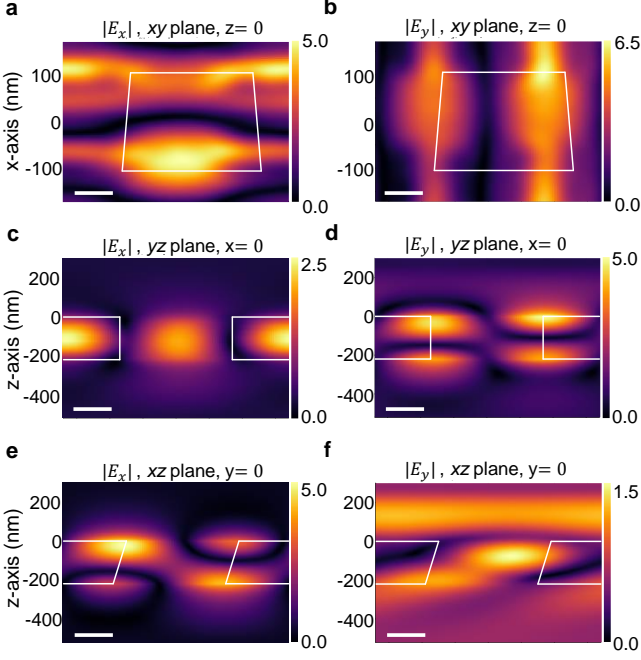


FIG. 1. **Electric field distribution of the BIC mode at $\lambda = 597$ nm.** **a,b** E_x and E_y in the xy -plane at the top surface, where we place our monolayer ($z=0$), respectively. **c-d** E_x and E_y components of the cross-sections in the (c - d) yz - and (e - f) xz -planes, at $x=0$ or $y=0$, respectively. The contour of the metasurface is marked as white solid lines. The scale bar size is 50 nm.

the exciton reservoir. The pumping rate χ is modeled within the random source model [2] as a random process satisfying

$$\langle \chi_\alpha(\mathbf{q}, t) \rangle = 0, \quad (8)$$

$$\langle \chi_\alpha^*(\mathbf{q}, t) \chi_\beta(\mathbf{q}', t') \rangle = \rho_{\alpha\beta}(\mathbf{q}, t) \delta_{\mathbf{q}, \mathbf{q}'} \delta(t - t') \quad (9)$$

where ρ_{ij} is defined both by the polarization of the pump and by the relaxation kinetics of excitons due to exciton-phonon and exciton-exciton interactions.

The equation (7) for \mathbf{P} can be solved exactly, and then \mathbf{P} can be substituted into Eq. (2) which results in the equation for the total field at $z = 0$ which again can be solved exactly. Finally, we obtain the expression for the far field electric field:

$$E_\alpha(\mathbf{k}, z \rightarrow \infty, \omega) = \quad (10)$$

$$G_{\mathbf{k}, \alpha\beta}^{0\mathbf{Q}}(-\infty, 0, \omega) [\hat{\alpha}_0(\mathbf{k} + \mathbf{Q}, \omega)^{-1} \quad (11)$$

$$\delta_{\mathbf{Q}\mathbf{Q}'} - \hat{G}_{\mathbf{k}}(0, 0, \omega)]_{\beta\xi}^{-1, \mathbf{Q}\mathbf{Q}'} \chi_\xi^{\mathbf{Q}'} / \gamma, \quad (12)$$

where α_0 is the bare exciton polarizability, $\alpha_0^{-1}(\mathbf{q}, \omega) = (\omega - \omega_X(\mathbf{q}) + i\Gamma - \frac{1}{2}\Omega_{\mathbf{q}}\sigma)$. We note that only the zero-th order diffraction order is accounted for in the far field, since the period of the structure is less than the wavelength. From Eq. (12) it can be seen that the eigenfrequencies and eigenmodes of the whole structure are given by the

condition $\text{Det} [\hat{\alpha}_0(\mathbf{k} + \mathbf{Q}, \omega)^{-1} - \hat{G}_{\mathbf{k}}(0, 0, \omega)] = 0$, and the profile of the polariton mode could be restored from the kernel vector of this matrix. The kernel vector has two components of in plane electric field for each diffraction order \mathbf{Q} . Therefore, we can image a polariton mode profile at specific \mathbf{k} as an image on the reciprocal lattice where each node depicts a polarization ellipse for specific diffraction order. These plots are shown in Figs. 2(a,b) for lower polariton mode at $\mathbf{k} = 0$. The red and blue colors correspond to two helicities with violet color depicting linear polarization. We can see that the helicity of the polariton near field η satisfies $\eta(\mathbf{Q}) = -\eta(-\mathbf{Q})$ due to time reversal symmetry. We also note that while for the achiral structure (without slant) the main diffraction orders are linearly polarized, for the chiral structure two main diffraction orders along y axes have finite and opposite helicities. The slant angle leads to the asymmetric scattering of $+1$ and -1 diffraction orders to far field which ultimately leads to the circularly polarized far field emission.

We can calculate the far-field intensity from the electric field and average it over the random sources yielding the final expression for the polarization resolved PL intensity $I_{\alpha, \alpha'}$

$$I_{\alpha'\alpha}(\mathbf{k}) = \gamma^{-2} R_{\alpha'\beta'}^{\mathbf{Q}'} \rho_{\beta', \beta}(\mathbf{k} + \mathbf{Q}', \omega) R_{\alpha\beta}^{\mathbf{Q}'}; \quad (13)$$

$$R_{\alpha\beta}^{\mathbf{Q}'} = G_{\alpha\xi}^{0\mathbf{Q}} (\hat{\alpha}_0^{-1} - \hat{G})_{\xi\beta}^{-1, \mathbf{Q}\mathbf{Q}'} \quad (14)$$

Equation (14) relates the far field emission intensity to the stationary distribution of the exciton pump rate ρ . We note that this distribution is qualitatively different from the thermal distribution since the system is out of equilibrium due to pump and radiative decay. Moreover, since the polaritons have negative effective mass, there can be no thermal equilibrium in the system. While precise determination of the distribution function would require the solution of Master equation for the density matrix accounting for the exciton-phonon and exciton-exciton scattering, we would adopt a generic expression for $\rho_{\alpha\beta}$:

$$\rho_{\alpha\beta}(\mathbf{q}, \omega) = \rho_{\alpha\beta}^{(0)} (1 - e^{-q^2/\tilde{q}^2}), \quad (15)$$

where $\rho^{(0)}$ is the polarization matrix of the optical pump, and \tilde{q} is the fitting parameter. The dependence in Eq. (15) reflects the suppression of the pump to $q = 0$ states and to relatively stronger pump to the high q state lying outside the light cone.

The calculated reflectivity and PL spectra based on our model for chiral (with slant) and achiral (without slant) geometries are presented in $2c - f$. The different underlying physics between reflectivity and PL spectra are seen in both cases, where the exciton response dominates the reflectivity spectrum, while the polariton emission dominates the PL spectrum. This shows that the PL intensity enhancement of polaritons is mainly owed to the Brillouin zone folding, overcoming thermalisation

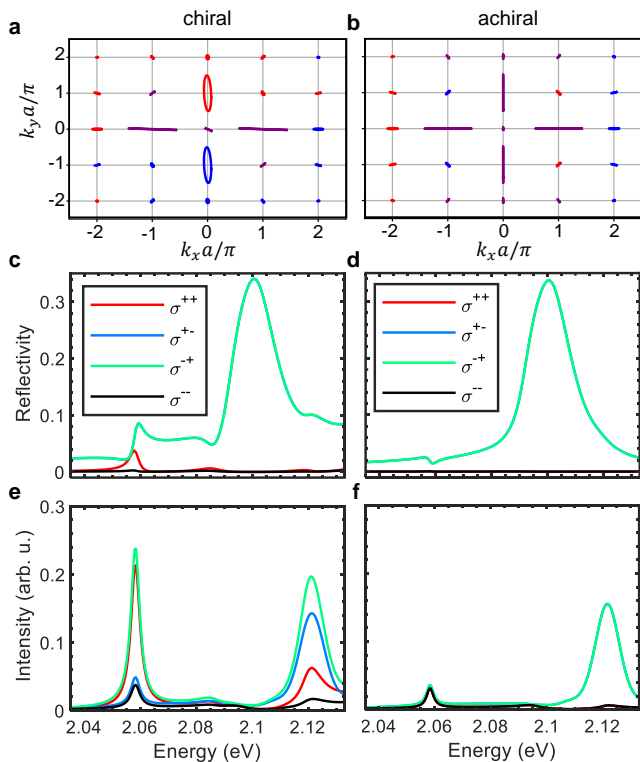


FIG. 2. **Modeled polarisation properties, and reflectivity and PL spectra of exciton-polaritons in (with slant) chiral and (without slant) achiral geometries.** **a,b** Polarisation of the lower polariton in the diffraction orders, with (blue) σ^- , (red) σ^+ and (purple) linear polarisation, and the ellipticity corresponding to the degree of circular polarisation, for chiral and achiral structures, respectively. **c,d** Polarisation resolved reflectivity spectra of the modeled chiral and achiral structures, respectively, where σ^{ir} convention indicates polarisations of the incoming (*i*) and reflected (*r*) light. **e,f** Polarisation resolved PL spectra of the modeled chiral and achiral structures, respectively, where σ^{pe} convention indicates polarisations of the pump (*p*) and emitted light (*e*).

as discussed in the main text, and as such, is independent on chirality. However, as especially seen for the lower polariton, the chiral geometry induces asymmetry between the spectra produced by σ^+ and σ^- polarised white and laser light, respectively. This behavior underlines the intrinsically chiral nature of the exciton polaritons forming in the strong coupling regime between chiral BIC photons and excitons.

Experiment: To probe polaritons and excitons in our system, we performed polarisation resolved PL and reflectivity measurements at normal incidence (see Fig. 3a-d)). Therefore, we employed either a circularly polarised cw-laser ($\lambda = 561nm$) or circularly polarised white light. For σ^+ polarised light sources (see Fig. 3a,b), the σ^+ polarised component of the emitted and reflected light yields a strong lower polariton peak. The σ^- component, on the contrary, stems mainly from the upper polariton

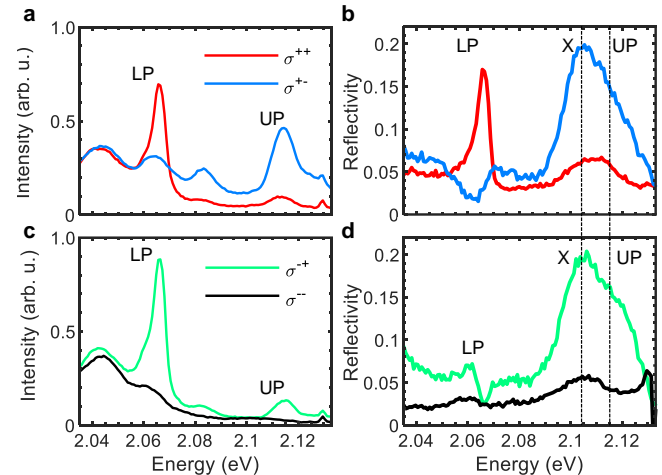


FIG. 3. **Polarisation resolved reflectivity and PL spectra of our structure.** **a,b** Polarisation resolved photoluminescence and reflectivity spectra at $k = 0$ using σ^+ polarised laser excitation or white light, respectively. **c,d** Polarization resolved photoluminescence and reflectivity spectra at $k = 0$ using σ^- polarised laser excitation or white light, respectively.

in the PL and from the exciton in the reflectivity measurement. This behavior changes dramatically for σ^- polarised light sources (see Fig. 3c,d), where contributions of excitons and polaritons are all strongest for the σ^+ polarised component of the emitted and reflected light, and suppressed for the σ^- polarised component. This results from the interplay between intrinsically chiral states and rotating dipoles, combined with diffraction induced photoluminescence, as discussed in the main text. As the lower polariton possess robust σ^+ -polarisation, independent on the polaritons of the pump, and is only receptive to σ^+ -polarised whitelight, we conclude that the lower polariton is an intrinsically chiral light-matter hybrid state, inheriting the physics from the intrinsically chiral photonic BIC [3].

-
- [1] J. Schlipf and I. A. Fischer, Rigorous coupled-wave analysis of a multi-layered plasmonic integrated refractive index sensor, *Optics Express* **29**, 36201 (2021).
 [2] L. Deych, M. Erementchouk, A. Lisyansky, E. Ivchenko, and M. Voronov, Exciton luminescence in one-dimensional resonant photonic crystals: A phenomenological approach,

- Physical Review B—Condensed Matter and Materials Physics **76**, 075350 (2007).
 [3] Y. Chen, H. Deng, X. Sha, W. Chen, R. Wang, Y.-H. Chen, J. C. Dong Wu, Y. S. Kivshar, S. Xiao, and C.-W. Qiu, Observation of intrinsic chiral bound states in the continuum, *Nature* **613**, 474–478 (2023).